Journal of Power Sources 185 (2008) 1168–1178

Contents lists available at ScienceDirect

Journal of Power Sources

journal homepage: www.elsevier.com/locate/jpowsour

Continuum-level solid oxide electrode constriction resistance effects

George J. Nelson [a], Comas L. Haynes [b,*]

[a] Woodruff School of Mechanical Engineering, Georgia Institute of Technology, Atlanta, GA 30332-0405, USA
[b] Georgia Tech Center for Innovative Fuel Cell and Battery Technologies, Atlanta, GA 30332-0853, USA

ARTICLE INFO

Article history:
Received 15 May 2008
Received in revised form 3 July 2008
Accepted 4 July 2008
Available online 22 July 2008

Keywords:
Solid oxide cell
SOFC
Constriction resistance
Transport phenomena

ABSTRACT

Continuum-level mass and electronic transport through solid oxide cell electrodes, inclusive of ribbed interconnects, are modeled employing analytical solutions of the 2D Laplace equation. These analytical solutions describe localized mass and electronic transport phenomena in solid oxide fuel cell (SOFC) anodes and localized mass transport phenomena in SOFC cathodes. Two-dimensional constriction resistance effects created by reductions in active transport area are shown to significantly increase internal cell resistances by increasing transport path lengths within a cross-sectional region of the cell. Furthermore, these effects can alter cell performance with respect to fuel depletion phenomena and create a competition of losses between mass and electronic transport resistances. Fuel depletion is shown to occur at a current density lower than the traditionally defined limiting current density. An analytical expression for this fuel depletion current density is proposed based upon the models developed. The competition between mass transfer and electronic resistance effects arising from solid oxide cell interconnect geometry is also characterized through parametric studies based on a design of experiments (DOEs) approach. These studies demonstrate the benefits of smaller SOFC unit cell geometry.

1. Introduction

Solid oxide cells are an environmentally attractive technology that could play a key role in the development of a more sustainable global energy infrastructure. Solid oxide cells are best known in the energy sector as novel power generation devices via solid oxide fuel cells (SOFCs), which enable the direct conversion of chemical energy to electrical energy. Through this direct conversion of chemical energy, SOFCs can circumvent many of the power generation losses associated with thermal and mechanical energy conversion methods. In addition to their direct energy conversion benefits, fuel cells produce fewer criteria pollutants than combustion-based technologies by operating below the temperature ranges associated with thermal NO_x formation and operating upon desulfurized fuels. Finally, SOFCs allow for more modular designs, cogeneration, and more flexible siting options than most of the current combustion-based technologies [1]. Effective modeling and simulation of solid oxide cell transport phenomena continues to be important, particularly with respect to the development of higher fidelity SOFC models that account for local transport effects. The present article reports an analytic approach for modeling local transport phenomena in solid oxide cells that focuses on constriction resistance in localized cross-sectional regions of the electrode component. Special attention is given to distortions in local transport phenomena that are caused by interconnect geometry.

Prevalent analyses of key SOFC transport phenomena are often conducted employing a herein-labeled "button-cell" approximation in which one-dimensional transport is presumed to occur within the SOFC electrodes, as illustrated in Fig. 1. This approximation is employed in both theoretical and experimental analyses [2–4]. In such analyses the effects of actual SOFC interconnect geometry are not directly addressed. Given a typical SOFC geometry with co-flow rectangular passageways, contact between the gas stream and electrode surface is restricted to a gas channel defined by the interconnect geometry. The change in mass transport cross-sectional area from the gas stream–electrode to the electrode–electrolyte interface, due to interconnect design, will result in significant deviations from the present button-cell idealization of mass transfer in SOFCs [5,6]. The reduction in cross-sectional area from the electrolyte–electrode interface to the electrode–interconnect interface also causes a distortion of electronic current [6,7]. This distortion increases ohmic losses. These additional resistances are due to the added path lengths associated with constriction resistance effects within the electrode.

The concept of constriction resistance is well-known within engineering practice, and is most commonly encountered in problems involving the study of thermal and electrical contact resistance. It was notably studied by Greenwood with respect to

* Corresponding author. Tel.: +1 404 407 7578; fax: +1 404 407 8520.
E-mail address: comas.haynes@gtri.gatech.edu (C.L. Haynes).

0378-7753/$ – see front matter © 2008 Elsevier B.V. All rights reserved.
doi:10.1016/j.jpowsour.2008.07.020

Nomenclature

a	unit cell half-width (m or cm)
ASR	electronic area specific resistance ($\Omega\,cm^2$)
b	fuel stream half-width (m or cm)
D_{ij}	binary diffusion coefficient ($m^2\,s^{-1}$)
F	Faraday constant ($C\,mol^{-1}$)
i''	local current density ($A\,m^{-2}$ or $A\,cm^{-2}$)
L_{FS}	fuel stream contact width (m or cm)
L_{Total}	unit cell total width (m or cm)
p	partial pressure (kPa)
R_u	universal gas constant ($kJ\,mol^{-1}\,K^{-1}$)
T	Temperature (K)
V	voltage (V)
$\bar{V}$	average voltage (V)

Greek symbols

ε	anode porosity
σ	electrical conductivity $(\Omega\,cm)^{-1}$
τ	tortuosity

Subscripts

an	bulk anode parameter
an–elec	anode–electrolyte interface
an–FS	anode–fuel stream interface
an–IC	anode–interconnect interface
ca–AS	cathode–air stream interface
ca	bulk cathode parameter
H_2	hydrogen
H_2O	steam
O_2	oxygen

constriction resistance caused by micro-contacts [8]. More contemporary studies of thermal and electrical contact resistance are also available [9–11]. The most express application of the concept of constriction resistance to the analysis of SOFC transport phenomena was conducted by Fleig and Maier, and later Fleig et al. [12,13]. In this work the authors used finite element analysis (FEA) to determine the effects of electrode–electrolyte contact upon potential distributions within the electrolyte layer of a solid oxide fuel cell. Ultimately, Fleig demonstrated that triple-phase boundaries at the electrode–electrolyte interface act as constrictions within the flow of current through the electrolyte and increase the electrolyte resistance [13].

While numerous efforts to more accurately model geometry effects have been made, those focused on developing analytical expressions for understanding geometry effects have involved general expressions for cell concentration and ohmic polarization and have typically relied upon a one-dimensional characterization of transport phenomena across the electrodes [2,14–16]. Analyses seeking a more detailed description of transport phenomena rely heavily upon numerical techniques, inclusive of computational fluid dynamics (CFD) and FEA, to ascertain the multidimensional characteristics of SOFC transport phenomena [5–7,12,13,17–20]. Ferguson et al. apply CFD techniques toward modeling thermal, mass, and electronic transport within solid oxide fuel cells and demonstrate the effects of interconnect rib size on cell performance. Ohmic losses are shown to be reduced by broader interconnect ribs. However, the interconnect is shown to reduce hydrogen concentration in regions not directly beneath the anode–fuel stream interface [6]. Ji et al., demonstrate similar effects on cathode mass transport [5]. A competition between ohmic and concentration polarization within the anode, arising from cell geometry, can be inferred from these results. More recently, Joshi et al. have examined SOFC mass transport using the Lattice Boltzmann method [21,22]. While these models address two-dimensional mass transport within SOFCs, emphasis is given to electrode geometry on the microstructural level. The cell-level effects of interconnect geometry addressed in the present work are not considered.

The present work develops a means of analyzing the effects of increased transport path lengths caused by constriction resistance in prevalent solid oxide cell designs, and explores constriction resistance effects within solid oxide cell electrodes through analytic solutions of the Laplace equation. Individual boundary value problems for localized electrode mass and electronic transport are proposed and solved independently. This approach allows for the consideration of constriction resistance effects that may arise from the design of specific electrode geometry. Furthermore, for a given SOFC anode geometry these solutions lead to the definition of a "fuel depletion" current density, which is distinct from the traditionally defined limiting current density. Finally, the models developed are employed in parametric studies of SOFC anode geometries. These studies, constructed using a design of experiments (DOEs) approach, demonstrate the potential benefits of smaller unit cell geometries.

2. Model formulation

2.1. Unit cell geometry

In the present work, a unit cell is defined as a single pair of co-flow reactant channels which encompass (or "sandwich") the corresponding solid oxide cell *positive electrode*/*electrolyte*/*negative electrode* (P–E–N) tri-layer, as shown in Fig. 1. The present work focuses on a cross-sectional region of the electrode components of this fundamental element of a full co-flow cell arrangement. For the models developed, the lengths a and b are defined as half the total unit cell width and half the fuel stream width, respectively. A symmetry boundary condition is applied about the centerline of the reactants channels to further simplify the problem geometry. Finally, a dimensionless length fraction (LF) is defined to compare the gas stream contact length to the total unit cell length:

$$a = \frac{L_{Total}}{2}; \quad b = \frac{L_{FS}}{2}; \quad LF = \frac{b}{a} = \frac{L_{FS}}{L_{Total}} \tag{1}$$

2.2. Potential flow models

2.2.1. Mass transport models

In steady-state operation solid oxide fuel cell geometry effects can be examined in a direct manner employing the analytic solution of the Laplace equation. This approach is applied toward the anodic voltage and partial pressure distributions, and the cathodic oxygen partial pressure distribution by the establishment of four boundary value problems: one for hydrogen transport, one for steam transport, one for the anodic voltage distribution, and one for oxygen transport. The application of a potential flow approach to the partial pressure problems is made possible primarily through the basic assumptions of equimolar counterdiffusion of hydrogen and steam within the anode, a stationary medium within the cathode, and relatively thin reaction zones ($\sim$10 μm) at the electrode–electrolyte interfaces [4]. The last of these assumptions is especially appropriate for the anode-side of the common anode-supported SOFC arrangement. For the cathode, the stationary medium and thin reaction zone assumptions produce a conservative (i.e., lower) estimate of the oxygen partial pressure distribution within the cathode. The conservative estimate of oxygen partial pressure causes a com-

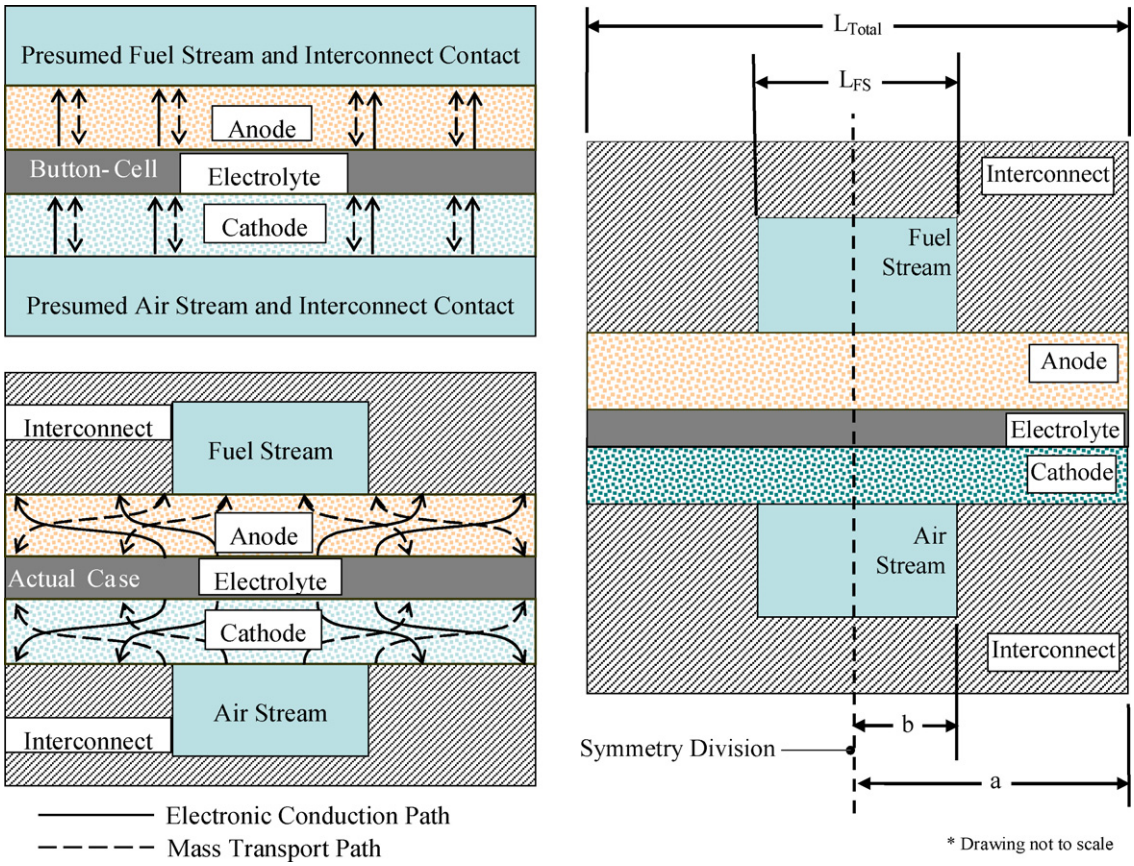

Fig. 1. Button-cell approximation, actual SOFC geometry and unit cell geometry employed in present analysis.

putational "safety factor" to result when designing for reduced cathodic concentration polarization.

A uniform partial pressure acrosss the gas channel cross-section is also assumed for the reactant gas species. This assumption is a result of anticipated low resistance to convective mass transport within the gas channel when compared to resistance to diffusion within the electrode. This assumption is corroborated through a brief comparison of the diffusive and convective mass transfer resistances, as defined in Eqs. (2) and (3):

$$R_{\text{Diff}} = \frac{t_{\text{anode}}}{D_{\text{H}_2-\text{H}_2\text{O}} A_s} \frac{\tau}{\varepsilon} \tag{2}$$

$$R_{\text{conv}} = \frac{d_h}{D_{\text{H}_2-\text{H}_2\text{O}} \cdot Sh \cdot A_s} \tag{3}$$

A_s is the surface area of the anode in contact with the fuel channel, and d_h is the hydraulic diameter. The binary diffusion coefficient for a hydrogen–steam mixture, $D_{\text{H}_2-\text{H}_2\text{O}}$, is defined using the Chapman–Enskogg model as outlined by Reid et al. [23]. The variables ε and τ are the anode porosity and tortuosity, respectively. Their ratio is the anodic permissivity, which is incorporated to create an effective diffusion coefficient as defined in [4]. It should be noted that the binary diffusion coefficient for the hydrogen–steam mixture is used in Eq. (3) because the convective mass transfer resistance relates to diffusion within the fuel stream, which would have a permissivity of 1.0.

For a standard flow channel width on the order of 1 mm and a nominal height of 1 mm, the ratio of convective resistance within the flow channel to conductive resistance within the electrode can be found using published Sherwood number values [24]. The convective mass transfer resistance within the fuel channel is 2–3% of the diffusive mass transfer resistance. Thus for the present model, the diffusive resistance is considered to be the dominant mass transfer resistance.

The stationary medium approximation within the cathode can be supported by the comparison of diffusive and molar average velocity effects stemming from the convection–diffusion equation, Eq. (4). Here, the molar average velocity and its respective magnitude are defined in Eq. (5). The magnitude of this velocity can be applied in the mass diffusion Peclet number.

$$\vec{J}_{O_2} = -D_{O_2-N_2} \frac{\varepsilon}{\tau} \vec{\nabla} C_{O_2} + \frac{C_{O_2}}{C_{\text{tot}}} \vec{J}_{O_2} \tag{4}$$

$$\vec{v} = \frac{\vec{J}_{O_2}}{C_{\text{tot}}} \Rightarrow \left|\vec{v}\right| = \frac{i''}{4FC_{\text{tot}}} = \frac{i'' R_u T}{4F p_{\text{tot}}} \tag{5}$$

$$Pe_m = \frac{L_c \cdot \left|\vec{v}\right|}{D_{O_2-N_2}} = Re_L Sc \tag{6}$$

Defining the characteristic length, L_c, as the ratio of cathode cross-sectional area to the perimeter of the cross-section, a comparison of diffusive and convective (molar average velocity) influences can be made. This comparison suggests the dominance of diffusion within the cathode and justifies the application of the stationary medium approximation. Additional comparisons based upon a characteristic length equal to the unit cell width add further support to this assumption.

It is important to note that present analyses are conducted for a two-dimensional cross-section of a SOFC electrode. While the effects of axial pressure drop, reactant consumption, and product formation along the length of the SOFC gas channel will also influence results, they are not considered in the present work.

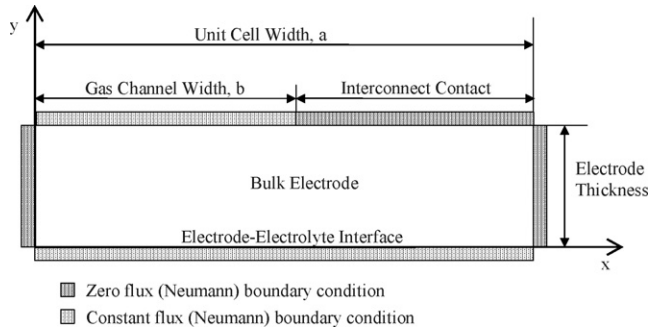

Fig. 2. General domain studied for potential flow model development, the bulk electrode may be the cathode or anode in contact with oxidant or fuel channels, respectively. The results in the present work pertain to local mass and electronic transport in the anode and local mass transport in the cathode.

This exclusion allows for the greater emphasis on the performance effects of local two-dimensional transport in the electrode components of SOFC unit cell cross-sections.

The boundary value problem for the hydrogen partial pressure is defined in Eqs. (7)–(10). This problem consists of the Laplace equation (no internal species generation) with constant species flux boundary conditions specified at the anode–electrolyte and anode–fuel stream interfaces. These boundary conditions, shown in Eqs. (8) and (9), are based upon an *a priori* assumption of uniform flux at the anode–electrolyte and anode–fuel stream interfaces of a localized cross-sectional region of the unit cell. The scaling factor, a/b, in Eq. (9) is the result of species conservation and the reduction in area between the respective interfaces. A zero species flux boundary condition is specified at the anode–interconnect interface. A corresponding problem can be defined for the steam partial pressure by reversing the sign of the boundary conditions given in Eqs. (8) and (9). The general domain studied in the development of the anode partial pressure model is shown in Fig. 2. A similar domain is used in the development of the anode voltage and cathode partial pressure models.

$$\frac{\partial^2 p_{H_2}}{\partial x^2} + \frac{\partial^2 p_{H_2}}{\partial y^2} = 0 \tag{7}$$

$$\frac{\partial p_{H_2}}{\partial y}(x,0) = \frac{R_u T}{2FD_{H_2-H_2O}} \frac{\tau_{an}}{\varepsilon_{an}} i'' = A_{0,an} \tag{8}$$

$$\frac{\partial p_{H_2}}{\partial y}(x,t_{an}) = \begin{cases} \dfrac{R_u T}{2FD_{H_2-H_2O}} \dfrac{a}{b} \dfrac{\tau_{an}}{\varepsilon_{an}} i'' & 0 < x < b \\ 0 & b < x < a \end{cases} \tag{9}$$

$$\frac{\partial p_{H_2}}{\partial x}(0,y) = 0, \quad \frac{\partial p_{H_2}}{\partial x}(a,y) = 0 \tag{10}$$

The solution to the hydrogen partial pressure problem is given in Eq. (11). The solution for the corresponding steam partial pressure distribution is given in Eq. (12). It is important to note that the sum of these solutions is equal to the set total pressure at all locations within the anode.

$$p_{H_2}(x,y) = p_{H_2,an-FS} - A_{0,an}(t_{an} - y) - \sum_{n=1}^{\infty} A_{n,an}[\cosh(\lambda_n t_{an}) - \cosh(\lambda_n y)\cos(\lambda_n x)] \tag{11}$$

$$p_{H_2O}(x,y) = p_{H_2O,an-FS} + A_{0,an}(t_{an} - y) + \sum_{n=1}^{\infty} A_{n,an}[\cosh(\lambda_n t_{an}) - \cosh(\lambda_n y)\cos(\lambda_n x)] \tag{12}$$

$$A_{n,an} = \frac{2A_{0,an}\,\sin(\lambda_n b)}{n\pi\lambda_n \sinh(\lambda_n t_{an})}\left(\frac{a}{b}\right); \quad \lambda_n = \frac{n\pi}{a} \tag{13}$$

Under the assumption of a stationary medium, the molar average term is removed from Eq. (4). The 1D solutions of this equation, with the stationary medium approximation applied, is shown in Eq. (14). The corresponding solution without the stationary medium approximation is shown in Eq. (15). Additionally, for a thin cathode a sufficient approximation for the one-dimensional pressure distribution can be made using the first terms from the series expansion of the exponential in Eq. (15), as shown in Eq. (16) [4]. It should be noted that Eqs. (14) and (16) differ only by the bracketed term. Thus the stationary medium approximation will under-predict the oxygen partial pressure when compared to the full solution, and is therefore considered a conservative estimate.

$$p_{O_2}(x) = p^o_{O_2} - \frac{i'' R_u T}{4FD_{O_2-N_2} p} \frac{\tau}{\varepsilon} x \tag{14}$$

$$p_{O_2}(x) = p - (p - p^o_{O_2})\,\exp\left[\frac{i'' R_u T}{4FD_{O_2-N_2} p} \frac{\tau}{\varepsilon} x\right] \tag{15}$$

$$p_{O_2}(x) \approx p^o_{O_2} - \left[\frac{p - p^o_{O_2}}{p}\right] \frac{i'' R_u T}{4FD_{O_2-N_2} p} \frac{\tau}{\varepsilon} x \tag{16}$$

The two-dimensional problem for cathode oxygen transport can be solved analytically if the stationary medium assumption is applied over the general domain shown in Fig. 2. This problem is established in the same manner as the hydrogen and steam problems. However, the boundary conditions at the horizontal boundaries require modification to account for the differing stoichiometric coefficient of oxygen, as shown in Eqs. (17) and (18). The resulting cathode oxygen pressure distribution is given in Eqs. (19) and (20):

$$\frac{\partial p_{O_2}}{\partial y}(x,0) = \frac{R_u T}{4FD_{O_2-N_2}} \frac{\tau_{ca}}{\varepsilon_{ca}} i'' = A_{0,ca} \tag{17}$$

$$\frac{\partial p_{O_2}}{\partial y}(x,t_{ca}) = \begin{cases} \dfrac{R_u T}{4FD_{O_2-N_2}} \dfrac{a}{b} \dfrac{\tau_{ca}}{\varepsilon_{ca}} i'' & 0 < x < b \\ 0 & b < x < a \end{cases} \tag{18}$$

$$p_{O_2}(x,y) = p_{O_2,ca-FS} - A_{0,ca}(t_{ca} - y) - \sum_{n=1}^{\infty} A_{n,ca}[\cosh(\lambda_n t_{ca}) - \cosh(\lambda_n y)\cos(\lambda_n x)] \tag{19}$$

$$A_{n,ca} = \frac{2A_{0,ca}\,\sin(\lambda_n b)}{n\pi\lambda_n \sinh(\lambda_n t_{ca})}\left(\frac{a}{b}\right); \quad \lambda_n = \frac{n\pi}{a} \tag{20}$$

2.2.2. Anode voltage model

A potential flow problem can also be solved to find the anode voltage distribution. Similar to the partial pressure case, the assumption of no internal charge generation is applied. Similar flux boundary conditions are applied, with the composite Neumann boundary condition Eq. (23) reversed to account for electrical contact at the anode–interconnect interface. The scaling factor seen in the denominator of Eq. (23) is the ratio of interconnect contact length to unit cell width. It can be derived by applying charge conservation to the anode domain and accounting for the reduction in area between the anode–electrolyte and anode–interconnect interfaces. The solution to the anode voltage problem is given in Eqs. (25) and (26):

$$\frac{\partial^2 V}{\partial x^2} + \frac{\partial^2 V}{\partial y^2} = 0 \tag{21}$$

$$\frac{\partial V}{\partial y}(x,0) = \frac{i''}{\sigma_{an}} \tag{22}$$

$$\frac{\partial V}{\partial y}(x,t_{an}) = \begin{cases} 0 & 0 < x < b \\ \dfrac{i''}{\sigma_{an}(1 - b/a)} & b < x < a \end{cases} \tag{23}$$

$$\frac{\partial V}{\partial x}(0,y)=0, \quad \frac{\partial V}{\partial x}(a,y)=0 \tag{24}$$

$$V(x,y)=\bar{V}_{\text{an-elec}}+\frac{i''}{\sigma_{\text{an}}}y+\sum_{n=1}^{\infty}A_n\ \cosh(\lambda_n y)\cos(\lambda_n x) \tag{25}$$

$$A_n=\frac{-2i''\ \sin(\lambda_n b)}{n\pi\sigma_{\text{an}}(1-b/a)\lambda_n\ \sinh(\lambda_n t_{\text{an}})}; \quad \lambda_n=\frac{n\pi}{a} \tag{26}$$

The average voltage at the anode–electrolyte interface, $\bar{V}_{\text{an-elec}}$, is defined by substituting Eq. (27) into Eq. (28) and solving for the interfacial voltage. The cathode lead voltage used in the present work was set at 1.0 V. Although this is an arbitrary setting, it facilitates the establishment of a numerical baseline for the desired analysis and is approximately representative of an ideal Nernst potential value. The standard Nernst potential is established as a temperature-dependent parameter using techniques outlined by Khaleel et al. [20]. The calculation of the Nernst potential, shown in Eq. (29), is defined to include anodic concentration losses. The ohmic resistance of the cathode and electrolyte component layers is taken from values provided in Zhao and Virkar [3]. The third and fourth terms in Eq. (28) represent the activation polarization as calculated via the Tafel Equation [4], with the exchange current density i_o and charge transfer coefficient α taken from available literature [25]. Temperature dependence of these latter two terms will influence cell performance with respect to activation polarization at lower current densities. However, an emphasis on the effects of geometric parameters was desired in the present analyses. So a constant temperature of 800 °C was established for all calculations, and constant activation polarization parameters were employed. The final term represents the cathodic concentration polarization. Where i''_{cs} is the limiting current density for the cathode as defined by Kim et al. [4] and shown in Eq. (30). Since this voltage model focuses on the anode, the cathode limiting current density is defined using the button-cell case. Future voltage models may include studies of *simultaneous* multidimensional mass transfer effects within both electrodes.

$$V_{\text{an,lead}}=\bar{V}_{\text{an-elec}}+i''\text{ASR}_{\text{an}} \tag{27}$$

$$\begin{aligned}V_{\text{cell}}=\ & V_{\text{ca,lead}}-V_{\text{an,lead}}\\ &=E^{\text{o}}-i''\text{ASR}_{\text{total}}-a_{\text{act}}-b_{\text{act}}\ \ln i''+\frac{R_{\text{u}}T}{4F}\ln\left[1-\frac{i''}{i''_{\text{cs}}}\right]\end{aligned} \tag{28}$$

$$E^{\text{o}}=-\frac{\Delta G}{2F}+\frac{R_{\text{u}}T}{2F}\ \ln\left[\frac{\bar{p}_{\text{H}_2,\text{an-elec}}}{\bar{p}_{\text{H}_2\text{O,an-elec}}}\right] \tag{29}$$

$$i''_{\text{cs}}=\frac{4FD_{\text{O}_2-\text{N}_2}}{R_{\text{u}}T}\frac{\varepsilon}{\tau}\frac{p_{\text{O}_2,\text{ca-AS}}}{t_{\text{ca}}}\left(\frac{p}{p-p_{\text{O}_2,\text{ca-AS}}}\right) \tag{30}$$

$$\begin{aligned}\bar{V}_{\text{an-elec}}=\ & 1-E^{\text{o}}+i''\text{ASR}_{\text{ca,elec}}\\ &+a_{\text{act}}+b_{\text{act}}\ \ln i''-\frac{R_{\text{u}}T}{4F}\ln\left[1-\frac{i''}{i''_{\text{cs}}}\right]\end{aligned} \tag{31}$$

2.2.3. Fuel depletion current density

The current drawn from a SOFC is ultimately limited by mass transfer within the electrode layers. For a given fuel stream partial pressure, a large enough current will cause hydrogen to be consumed at the anode–electrolyte interface faster than it can be sustainably supplied by the fuel stream. This scenario is referred to as fuel depletion and leads to fuel starvation, or the absence of fuel at the anode–electrolyte interface. In these fuel-depleted regions the lack of hydrogen, in conjunction with the electro-oxidative generation of oxygen, can promote transformation of the Ni phase back into NiO [15]. Such a redox scenario could have deleterious effects on SOFC performance and reliability, specifically with respect to changes in anodic microstructures compromising interfacial integrity [26].

Given a conventional interconnect design (Fig. 1), the onset of fuel depletion at the anode–electrolyte interface is expected to occur at the interconnect rib midpoint. A fuel depletion current density, i''_{FD}, can be defined by solving the expression for "zero" hydrogen partial pressure at this point ($x=a$, $y=0$) for the corresponding current density.

$$i''_{\text{FD}}=\frac{2FD_{\text{H}_2-\text{H}_2\text{O}}}{R_{\text{u}}T}\frac{\varepsilon}{\tau}\frac{p_{\text{H}_2,\text{an-FS}}}{t_{\text{an}}+\sum_{n=1}^{\infty}B_n\left[\cosh(\lambda_n t_{\text{an}})-\cos n\pi\right]} \tag{32}$$

$$B_n=\frac{A_{n,\text{an}}}{A_{0,\text{an}}}=\frac{2\sin(\lambda_n b)}{n\pi\lambda_n\ \sinh(\lambda_n t_{\text{an}})}\left(\frac{a}{b}\right) \tag{33}$$

If the button-cell approximation is applied (i.e., $b=a$), the constant B_n defined in Eq. (33) is zero. In this case, the fuel depletion current density defined by the anode partial pressure model approaches the more commonly defined limiting current density, Eq. (34). However, in actual SOFC operation the fuel depletion current density will be less than the expected limiting current density. This distinction is significant, since fuel-depleted operation may occur at current densities considered safe using a button-cell approach.

$$i''_{\text{FD}}=i''_{\text{lim}}=\frac{2FD_{\text{H}_2-\text{H}_2\text{O}}}{R_{\text{u}}T}\frac{\varepsilon}{\tau}\frac{p_{\text{H}_2,\text{an-FS}}}{t_{\text{an}}} \tag{34}$$

2.3. Anode design of experiments

A design of experiments approach was applied to develop parametric studies of the anode mass and electronic transport models using the commercially available statistical analysis software JMP (SAS Institute). Central composite experimental designs were established for four model responses: hydrogen fractional pressure drop, fuel depletion current density, anode area specific resistance, and anode lead voltage. This central composite design (CCD) was achieved by calculating the model output parameters at the minimum, midpoint, and maximum values of the input variables used in the design of experiments studies. Additionally, model outputs were calculated at random points throughout the design space to achieve a better characterization of model behavior.

3. Model results and discussion

3.1. Initial potential flow results

3.1.1. Mass transport models

The potential flow models for hydrogen and steam transport were initially examined for a SOFC unit cell width of 1.0 mm and an anode thickness of 750 μm. A current density of 1.0 A cm^{-2} was applied at a cell temperature of 800 °C (1073 K). A binary mixture of 90% hydrogen and 10% steam at atmospheric pressure was used to model the fuel stream. An anodic porosity of 30% was assumed, and a tortuosity of 14.5 was used based on existing literature [4]. While this value is higher than geometric anode tortuosities measured experimentally (typically 2–10), it is estimated directly from experimental SOFC button-cell performance. It has been suggested that estimation of such heightened tortuosities may be mitigated by accounting for separate diffusion resistances within the bulk anode and the chemically active regions near the anode–electrolyte interface [3], by factoring in Knudsen diffusion within the anode [4], or by considering surface diffusion effects at the anode–electrolyte interface [27]. These effects are not considered in the present work. However, future analyses may incorporate such transport effects.

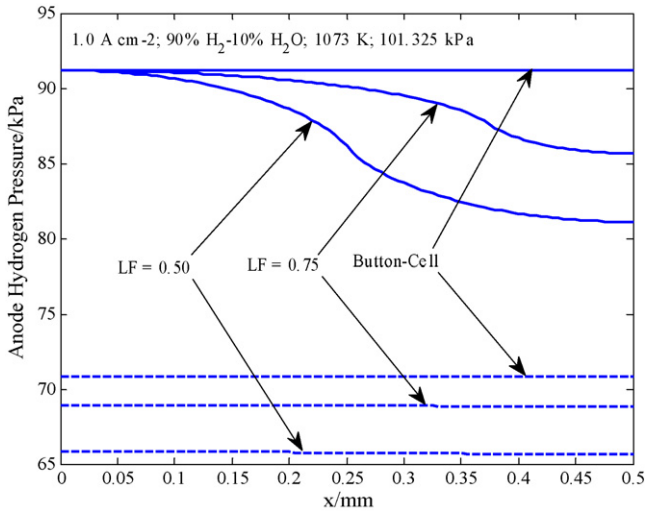

Fig. 3. Anodic hydrogen partial pressures for button-cell and actual cell geometries at the fuel stream/interconnect (–) and electrolyte (- -) interfaces.

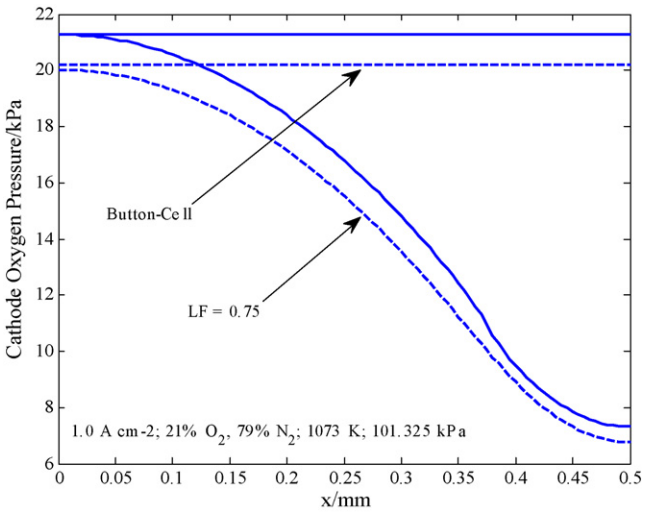

Fig. 5. Oxygen partial pressures for button-cell and actual cell geometries at the air stream/interconnect (–) and electrolyte (- -) interfaces.

In the present work the higher value is employed as an effective tortuosity for SOFC operation.

The hydrogen and steam partial pressure distributions for the button-cell and actual interconnect geometry cases are compared in Figs. 3 and 4. In these figures the solid and dashed lines indicate the pressure distribution along the electrode–interconnect/gas stream interface and the electrode–electrolyte interface, respectively. The influence of interconnect geometry is readily discernible. The hydrogen partial pressure at the anode–electrolyte interface is reduced when accounting for interconnect geometry. Correspondingly, the steam partial pressure at the anode–electrolyte interface shows a subsequent increase. Checks of the partial pressure distributions within the anode, as shown in Figs. 3 and 4, reveal that the sum of the hydrogen and steam partial pressures throughout the anode adds to atmospheric (i.e., the total) pressure. This condition was also found to be true for the other geometries analyzed in the present work.

Applying the model developed for the oxygen pressure distribution results in more drastic geometry effects, as shown in Fig. 5. Again, the solid and dashed lines indicate the electrode–interconnect/gas stream interface and the electrode–electrolyte interface. As with the anode pressure distributions, a unit cell width of 1.0 mm and a current density of 1.0 A cm^{-2} were used. A cathode thickness of 50 μm was used to reflect an anode-supported arrangement. Under the presumed one-dimensional transport of the button-cell case the pressure drop is relatively small compared to the anode, less than 1 kPa. However, a significant pressure drop along the width of the unit cell becomes evident when interconnect geometry is considered. Furthermore, at the edges farthest from the oxidant stream the cathode approaches oxygen depletion. In fact, for the cathode, results for LF = 0.50 are not shown since this geometry was found to experience depletion along a significant portion of the cathode–electrolyte interface. Under presumed 1D transport an anode-supported cell can be considered to be chiefly limited by the anode geometry, but for actual anode-supported SOFCs with conventional interconnects, the thinner cathode could in fact limit performance. This is associated with the increased in-plane (or "sheet") resistance effects. Performance limiting effects within the cathode have been demonstrated in numerical models of electrolyte-supported cells [5].

The effect of length fraction on hydrogen partial pressure drop within the anode is shown in Fig. 6 for several anode thicknesses.

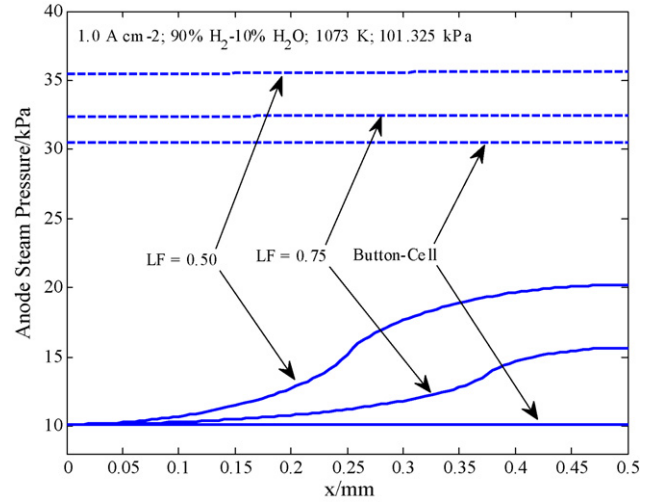

Fig. 4. Anodic steam partial pressures for button-cell and actual cell geometries at the fuel stream/interconnect (–) and electrolyte (- -) interfaces.

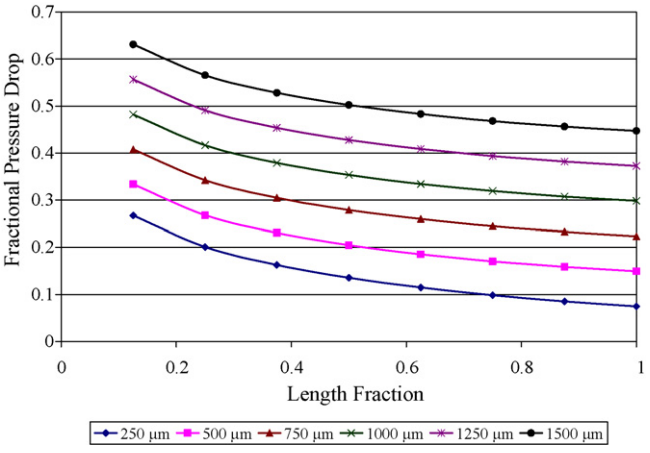

Fig. 6. Variation of hydrogen fractional pressure drop with length fraction for several anode thicknesses (The smallest geometry demonstrates an increased sensitivity to length fraction due to the influence of "sheet" resistance.).

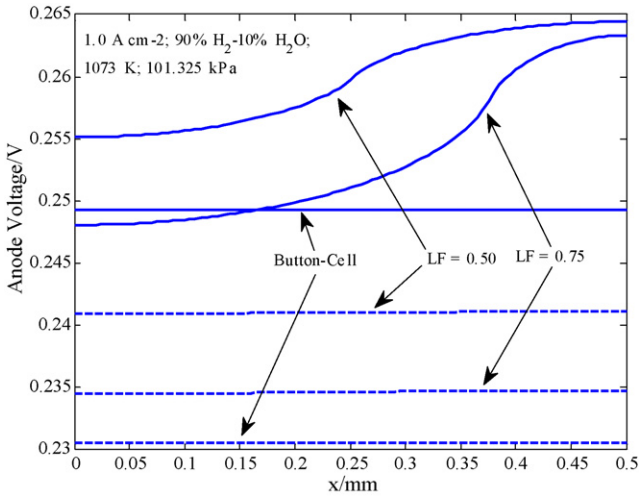

Fig. 7. Comparison of anodic voltage distributions for button-cell and actual cell geometries (The button-cell case for full electrical contact corresponds to LF = 0.).

In each case shown the current density was set at 1.0 A cm^{-2}, and a unit cell width of 1.0 mm was used. Again, a binary mixture of 90% hydrogen and 10% steam was modeled as the fuel stream. The values for a length fraction of one represent the button-cell case for mass transport (full fuel stream contact). The partial pressure drop was calculated as the difference between the fuel stream hydrogen partial pressure per the prescribed fuel stream pressure and composition, and the average anode–electrolyte interfacial partial pressure. This average was calculated from values obtained using Eq. (11). Overall, a decrease in length fraction results in an increase in resistance to the transport of hydrogen. It can be seen that the geometry effects are significant with the fractional pressure drop, the decrease in the average hydrogen partial pressure between fuel stream and the anode–electrolyte interface divided by the fuel stream hydrogen partial pressure, increasing approximately 20% when accounting for the nominal interconnect geometry. Resistance increases with anode thickness, and thinner anode geometries show an increased sensitivity to changes in length fraction, as indicated by a larger change in fractional pressure drop over the range of length fraction values. The former trend regarding anode thickness is intuitive for a fixed unit cell width (1.0 mm in the cases shown). The increased sensitivity of thin anodes can be attributed to the heightened impact of in-plane, or "sheet," resistance given smaller transverse resistances of thin anodes. In previous work these affects were shown to be more pronounced for a larger 2.0-mm unit cell width [28].

3.1.2. Anode voltage model

The anode voltage distributions for the button-cell and two interconnect geometry cases are compared in Fig. 7, with solid and dashed lines indicating the electrode–interconnect/gas stream interface and the electrode–electrolyte interface, respectively. As in the mass transport case, significant geometry effects can be seen. It is important to note that electrical contact only occurs over a select portion of the anode–fuel stream/interconnect interface (e.g. between 0.25 and 0.5 mm for LF = 0.50). Thus a higher voltage drop occurs across the anode when accounting for geometry effects. Furthermore, a general increase in anode lead voltage results from accounting for cell geometry. This increase will ultimately result in a decreased total cell voltage as defined in Eq. (27). Finally, it is noted that the smaller contact length for LF = 0.75 results in a marginally lower anode lead voltage. This small change in voltage can be attributed to enhanced mass transport that results from the larger fuel stream contact area, as shown in Fig. 3.

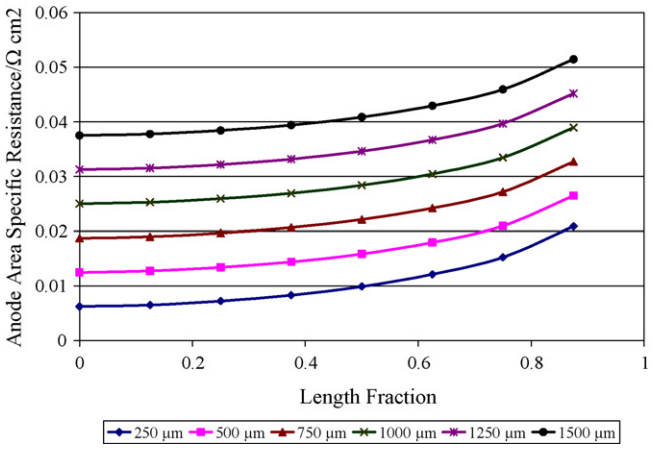

Fig. 8. Variation of anode ASR and with length fraction for several anode thicknesses.

In previous work, anode area specific resistances for the button-cell case calculated using potential flow models have been shown to agree well with values calculated from experimental models [28]. This agreement results from the 2D potential flow models reducing to the common 1D models in the button-cell case ($b = a$). However, accounting for actual geometry results in an increase in anode ASR, and non-linear behavior at lower anode thicknesses. Both of these effects can be attributed to the increased presence of sheet resistance effects.

Length fraction effects on anode electronic transport are shown in Fig. 8. The anode area specific resistance for an anode thickness of 750 μm (LF = 0.50) increases by ~18% when accounting for actual interconnect geometry. The anode area specific resistance is also shown to increase with length fraction. As in the hydrogen transport case, total resistance increases with anode thickness and demonstrates an increased sensitivity to length fraction for thinner anodes.

As seen in Figs. 6 and 8, a larger fuel stream contact area, represented by increasing length fraction, decreases mass transfer resistance and increases electronic resistance. Similarly, decreasing fuel stream contact reduces electronic resistance while increasing mass transfer resistance. Overall, the resistance to mass transfer displays a greater sensitivity to changes in interconnect geometry. Thus, mass transfer resistance effects are expected to limit anode transport phenomena more so than electronic resistance effects.

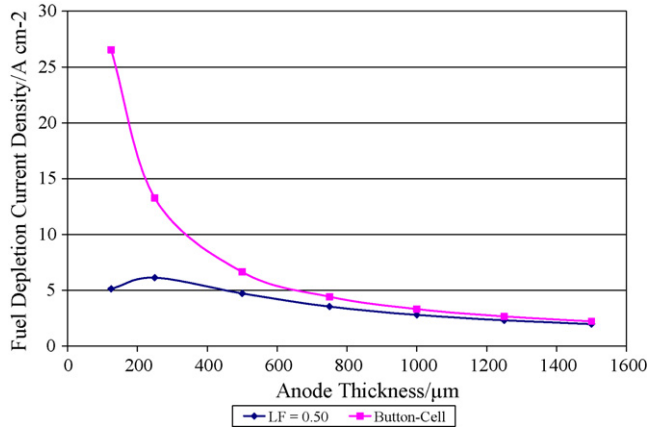

Fig. 9. Effects of interconnect geometry on fuel depletion current density.

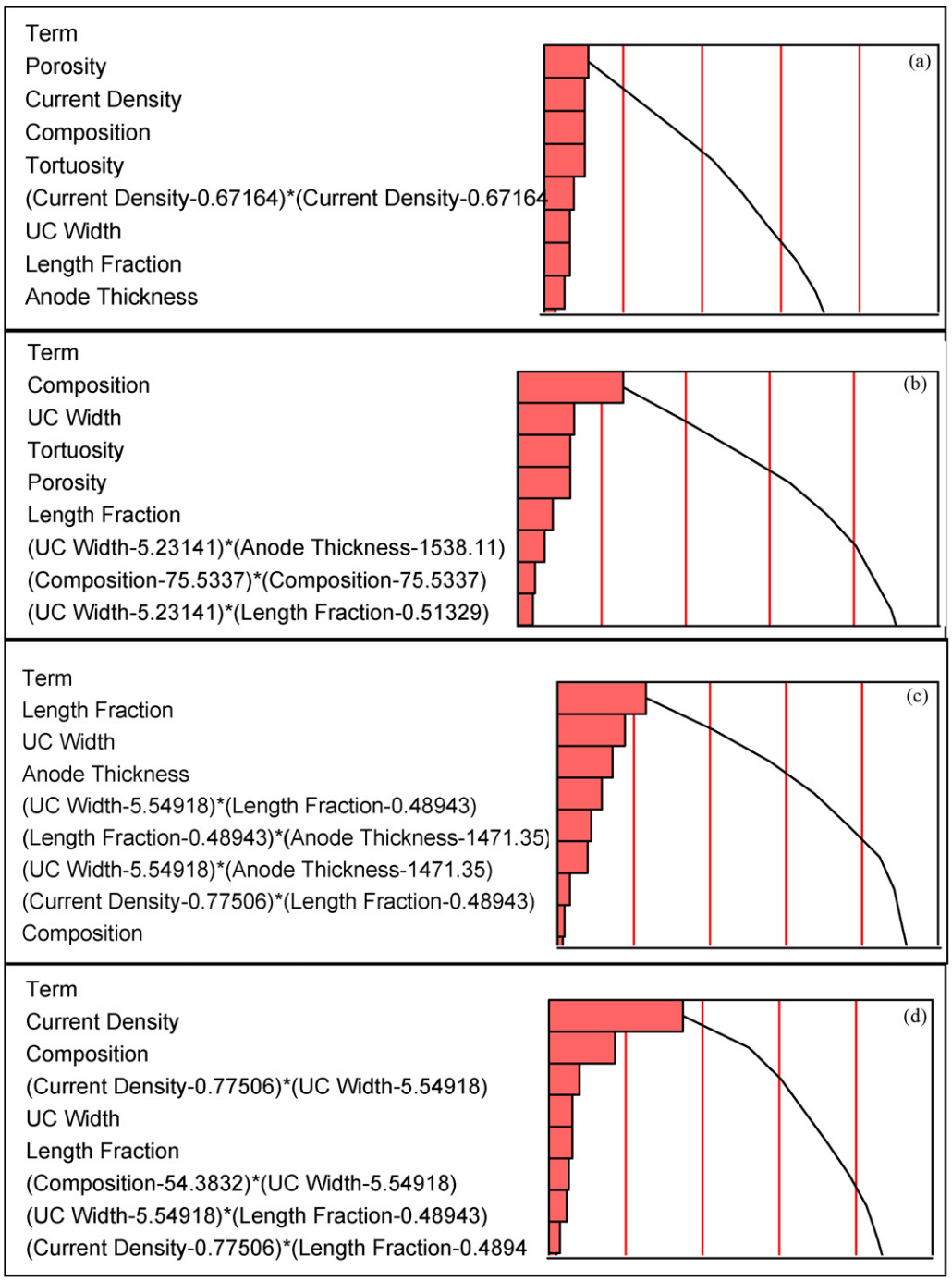

Fig. 10. Pareto plots demonstrating design variable influence on (a) fractional pressure drop (b) fuel depletion current density (c) anodic ASR and (d) anode lead voltage.

3.1.3. Fuel depletion current density

The ramifications of a fuel depletion current density are particularly important when considering the effects of interconnect geometry as demonstrated in Fig. 9. Under the button-cell approximation, the fuel depletion current density corresponds to the established definition of limiting current density, and is predicted to increase significantly as the anode becomes thinner. However, when interconnect geometry is accounted for (as shown for a length fraction of 0.50) the fuel depletion current density decreases after the thickness decreases below 500 μm *in the present study*. The cases shown in Fig. 9 are for a unit cell width of 1.0 mm. The change in behavior of fuel depletion current density as a function of anode thickness (in the case with LF = 0.50) can be attributed to the dominance of sheet resistance effects within the total anodic resistance to mass transfer. This concept was demonstrated above for the cathode oxygen partial pressure investigation. For excessively thin electrodes, the predominance of sheet resistance effects hindering mass transfer can become a significant performance issue. Again, comparable results for a larger unit cell geometry have been shown in previous work [29].

The fuel depletion current density values shown in Fig. 9 were calculated assuming an anodic tortuosity of 14.5, as predicted by

Kim et al. [4]. As noted, this value is significantly higher than common values of 2–10. The higher, effective tortuosity applied in these calculations produces fuel depletion current density values that are closer in magnitude to typical limiting current densities.

3.2. Anode design of experiments

Results of the design of experiments are outlined in the Pareto plots shown in Fig. 10. These plots provide a comparison of the relative influence of design variables on a given model response, ranking the influence of design variables in descending order. In some cases, a design variable may also influence model output in conjunction with other design variables, as shown through nonlinear functions present on each plot. For fractional pressure drop (Fig. 10a), the anode porosity and tortuosity, the fuel stream hydrogen composition, and the current density demand exert the primary influence over cell performance. These variables establish the primary characteristics of the hydrogen transport problem. In the case of fuel depletion current density (Fig. 10b), the fuel stream hydrogen composition exerts the greatest influence with unit cell width, porosity, and tortuosity demonstrating secondary levels of influence. The increased influence of the unit cell width may seem counterintuitive. However, this higher level influence can be linked to the presence of the unit cell half-width, a, within the eigenvalues of the solutions for the partial pressure distributions, λ_n. For the anode ASR (Fig. 10c), the geometric factors of length fraction, unit cell width, and anode thickness demonstrate the greatest influence over performance. The influence of the length fraction and unit cell width in this case can be linked to the calculation of the anode ASR, which is based upon the average voltage across the anode–interconnect contact surface. The size of this boundary is directly determined by the length fraction and unit cell width. Furthermore, the unit cell half-width, a, is again present within the eigenvalues of the solution for the anodic voltage distribution. Finally, the anode lead voltage, shown in Fig. 10d, has a primary dependence on current density, with a secondary dependence on fuel stream composition.

3.3. SOFC anode parametric studies

Parametric studies based on the above designs of experiments have been conducted. All results shown share the following (constant) parameters: anode thickness (750 μm), temperature (1073 K), and anode porosity and effective tortuosity (0.30 and 14.5, respectively). For a local current density, the effects of fuel stream hydrogen composition on fractional pressure drop, fuel depletion current density, and anode lead voltage were examined for three representative unit cell widths (1.0, 5.0, and 10 mm) and three representative length fraction values (0.125, 0.50, and 0.875). For these same geometries, the effects of local current density on fractional pressure drop and anode lead voltage were examined at a constant fuel stream composition. Finally, length fraction effects on anodic ASR were examined for the three representative unit cell sizes.

For the unit cell geometries analyzed, representative values of the fuel depletion current density computed for a range of fuel stream compositions are given in Table 1. All values shown are calculated for an anode thickness of 750 μm. The advantage of smaller unit cell geometries is apparent. For example, at all concentrations shown a SOFC with a unit cell width of 1.0 mm can achieve fuel depletion current densities approximately three times greater than those achieved by a SOFC with a unit cell width of 5.0 mm. The same 1.0-mm unit cell SOFC can achieve fuel depletion current densities almost 10 times greater than those achieved with a SOFC with a 10-mm unit cell. Furthermore, for the smallest geometry the onset of fuel depletion can occur at a current density

Table 1
SOFC fuel depletion current density over a range of fuel stream (FS) compositions

FS hydrogen composition (%)	SOFC fuel depletion current density ($A\,cm^{-2}$)		
	1.0 mm	5.0 mm	10 mm
5	0.20	0.06	0.02
10	0.40	0.13	0.04
50	1.98	0.63	0.20
90	3.57	1.13	0.36
95	3.77	1.20	0.38

near the traditionally defined limiting current density. As demonstrated in Fig. 11a, the onset of fuel depletion in such smaller width geometries corresponds to what is almost the complete absence of hydrogen at the anode–electrolyte interface. This scenario stands in sharp contrast to that of the larger 10-mm unit cell geometry shown in Fig. 11b. In the latter case the unit cell width serves as the greatest distance for hydrogen diffusion and results in a significant pressure drop in the lateral direction and a relatively low pressure drop between points across the anode thickness. Thus, for a given fuel stream composition and current density demand, a larger unit cell may exhibit a lower average pressure drop between the fuel stream and anode–electrolyte interface. However, these larger geometries may be noticeably more susceptible to fuel depletion at the anode–electrolyte interface.

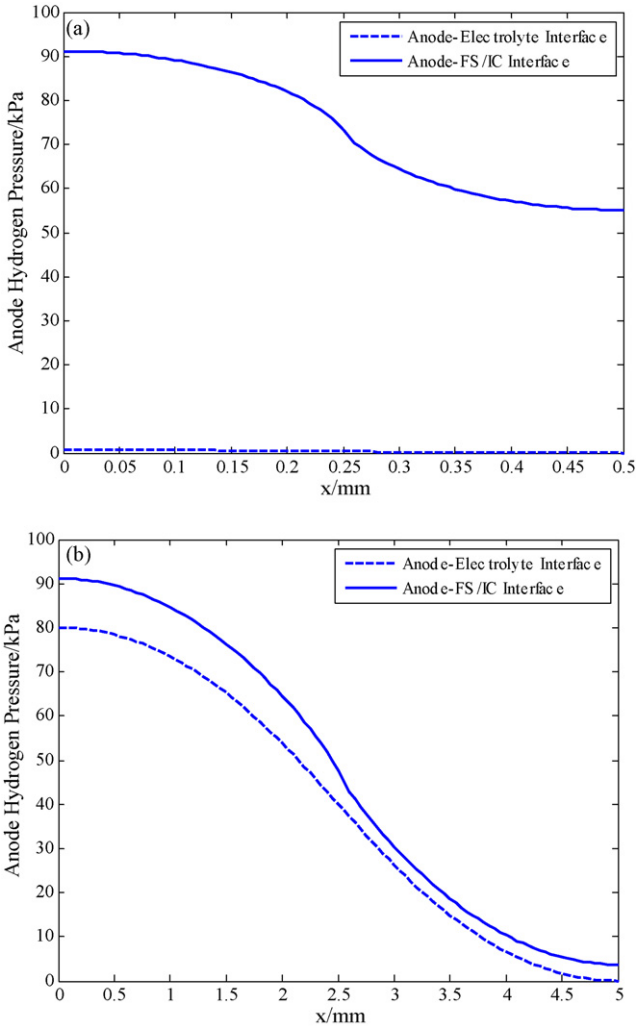

Fig. 11. Hydrogen partial pressure distributions at the fuel depletion current density for unit cells of (a) 1.0-mm width and (b) 10-mm width (90% fuel stream hydrogen).

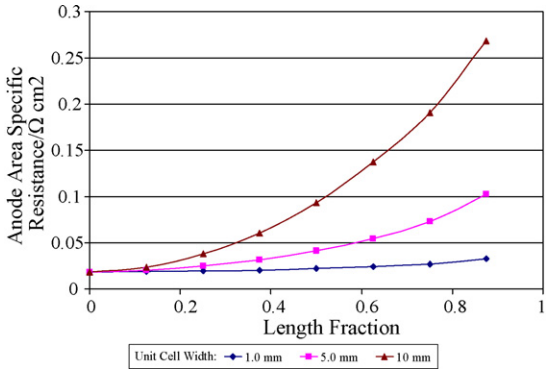

Fig. 12. Anode ASR as a function of length fraction for several unit cell sizes.

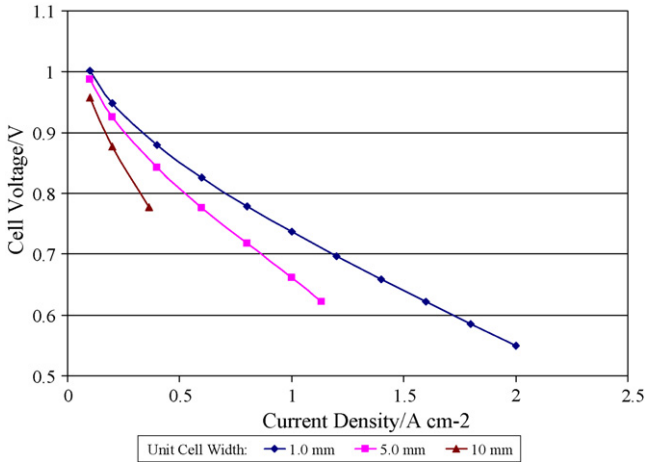

Fig. 13. Voltage–current density characteristics of several SOFC unit cell geometries for a 90% H_2, 10% steam fuel stream mixture.

Here, it is important to note that while the severe pressure drop in the lateral direction could be mitigated for larger unit cell geometries by increasing anode thickness, the analysis of such geometries is not desirable within the present work. State-of-the-art SOFC design has tended toward thin anode–electrolyte–cathode structures, with typical anode thicknesses between 250 and 2500 μm. Within this range, anode-supported SOFCs typically employ anodes of 500–1500 μm in thickness.

Finally, the advantage of smaller unit cell widths can be seen through a comparison of the effects of unit cell geometry on electronic transport phenomena in localized regions of the anode. The effects of interconnect geometry on anode ASR are shown in Fig. 12. As noted above, the smallest unit cell geometry shows an ~18% increase in ASR when comparing the button-cell case to the case with LF = 0.50. This relatively small increase contrasts the much larger increases in ASR seen for the 5- and 10-mm unit cells. These increased ASR values lead to predictions of diminished performance for larger unit cell geometries, as demonstrated by the voltage–current density characteristics in Fig. 13. These larger geometries also show greater limitations with respect to fuel depletion, as is evident in the limited range of operation displayed.

4. Conclusions

Resistance effects that arise from increased transport path lengths within solid oxide cells that utilize conventional ribbed interconnects have been analyzed through analytical models of mass and electronic transport phenomena. These resistance effects are collectively referred to as constriction resistance effects because the increase in transport path length directly results from reductions in active transport area that arise from solid oxide cell interconnect and anode design. The studies of these geometry effects focused on the effects of gas channel and interconnect contact lengths on localized mass and electronic transport within cross-sectional regions in the solid oxide fuel cell anode. Effects on localized mass transport were also modeled for cross-sectional regions of the cathode.

The transport within the electrode layers of a solid oxide fuel cell was examined using analytical solutions of the Laplace equation for mass and electronic transport. The solutions obtained show that significant resistance effects can be attributed to actual SOFC interconnect geometry in comparison to the common button-cell assumption. For SOFC anodes these effects were demonstrated to create a competition between mass and electronic transport losses. Effects on cathode oxygen transport were more dramatic, due to the thinner electrode geometry (50-μm thick) contributing more substantially to increased sheet resistance. Additional modeling of cathode electronic transport may be considered in future work.

In addition to showing the significance of geometry effects, the analytical model for hydrogen transport allows for the unique definition of a modified concept of limiting current density, called a "fuel depletion" current density. This performance metric accounts for SOFC geometry when modeling actual cell geometry and reduces to the standard definition of limiting current density *when applying a button-cell approximation*. However, the fuel depletion current density does not vary with anode thickness in the same way as the traditionally defined limiting current density. Specifically, reducing anode thickness does not invariably increase the fuel depletion current density. For thin anodes increased sheet resistance effects will result in a decrease in the current density that can be achieved prior to the onset of fuel depletion at the anode–electrolyte interface. A similar phenomenon is expected on the cathode side with respect to oxygen depletion.

The minimization of geometric resistance effects through the proper sizing of the fuel stream–anode and anode–interconnect contact areas was explored initially through parametric studies developed from a design of experiments approach. These parametric studies demonstrated the benefits of smaller SOFC unit cell widths. A unit cell was defined as the "sandwich" of a co-flow fuel stream interconnect channel and oxidant stream interconnect channel bounding a portion of the SOFC P–E–N tri-layer. Unit cell geometries with smaller widths were shown to experience lower ohmic losses and higher fuel depletion current densities. Furthermore, increasingly narrow unit cell geometries achieve cell voltages that are significantly higher than those of SOFCs with larger unit cell geometries. This superior performance is attributed to the reduced influence of sheet resistance effects in narrower unit cell geometries, when a constant anode thickness is maintained.

References

[1] N.Q. Minh, J. Am. Ceram. Soc. 76 (3) (1993) 563–588.
[2] S.H. Chan, Z.T. Xia, J. Appl. Electrochem. 32 (3) (2002) 339–347.
[3] F. Zhao, A.V. Virkar, J. Power Sources 141 (1) (2005) 79–95.
[4] J.-W. Kim, et al., J. Electrochem. Soc. 146 (1) (1999) 69–78.
[5] Y. Ji, et al., J. Power Sources 161 (1) (2006) 380–391.
[6] J.R. Ferguson, J.M. Fiard, R. Herbin, J. Power Sources 58 (2) (1996) 109–122.
[7] Y. Lin, S.B. Beale, Appl. Math. Model. 30 (11) (2006) 1485–1496.
[8] J.A. Greenwood, Br. J. Appl. Phys. 17 (12) (1966) 1621–1632.
[9] A.F. Black, V. Singhal, S.V. Garimella, J. Thermophys. Heat Transf. 18 (1) (2004) 30–36.
[10] A.A. Rostami, A.Y. Hassan, P.C. Lim, Heat Mass Transf. 37 (1) (2001) 5–10.
[11] R.S. Timsit, IEEE Trans. Compon. Pack. Technol. 22 (1) (1999) 85–98.
[12] J. Fleig, J. Maier, The influence of inhomogeneous potential distributions on the electrolyte resistance in solid oxide fuel cells, in Fifth International Symposium on Solid Oxide Fuel Cells (SOFC-V). 1997: Aachen, Germany.

[13] J. Fleig, et al., Solid State Ionics 113–115 (1998) 739–747.
[14] C.W. Tanner, A.V. Virkar, J. Power Sources 113 (1) (2003) 44–56.
[15] R.S. Gemmen, C.D. Johnson, J. Power Sources 144 (1) (2005) 152–164.
[16] Z. Lin, J.W. Stevenson, M.A. Khaleel, J. Power Sources 117 (1–2) (2003) 92–97.
[17] G.L. Hawkes, et al., CFD Model of a Planar Solid Oxide Electrolysis Cell for Hydrogen Production from Nuclear Energy, in The 11th International Topical Meeting on Nuclear Reactor Thermal-Hydraulics (NURETH-11). 2005: Avignon, France.
[18] S. Campanari, P. Iora, Fuel Cells 5 (1) (2005) 34–51.
[19] K. Sudaprasert, R.P. Travis, R.F. Martinez-Botas, Proc. Inst. Mech. Eng. A: J. Power Energy 219 (3) (2005) 159–167.
[20] M.A. Khaleel, et al., J. Power Sources 130 (1-2) (2004) 136–148.
[21] A.S. Joshi, et al., J. Power Sources 164 (2) (2007) 631–638.
[22] A.S. Joshi, et al., J. Phys. D: Appl. Phys. 40 (23) (2007) 7593–7600.
[23] R.C. Reid, J.M. Prausnitz, T.K. Sherwood, The Properties of Gases and Liquids, 3rd ed., McGraw-Hill, New York, 1977.
[24] F.P. Incropera, D.P. DeWitt, Fundamentals of Heat and Mass Transfer, 5th ed., John Wiley and Sons, New York, 2002.
[25] R.S. Gemmen, J. Fluid Eng. 125 (2003) 576–585.
[26] D. Waldbillig, A. Wood, D.G. Ivey, J. Power Sources 145 (2005) 206–215.
[27] R.E. Williford, et al., J. Electrochem. Soc. 150 (8) (2003) 1067–1072.
[28] G. Nelson, C. Haynes, Localized constriction resistance effects upon SOFC transport phenomena, in 2005 ASME International Mechanical Engineering Congress and Exposition (IMECE2005). 2005: Orlando, FL, United States.
[29] G. Nelson, C. Haynes, Parametric studies of constriction resistance effects upon solid oxide cell transport, in 2006 ASME International Mechanical Engineering Congress and Exposition (IMECE2006). 2006: Chicago, IL, United States.